

# NUMERICAL ANALYSIS OF WAKE THERMAL FLOW FIELD FOR SW300 PRO AERO-ENGINE

by

*Miao GONG<sup>\*1</sup>, Yuanhang SHEN<sup>1</sup>, Wen HUANG<sup>1</sup>*

<sup>\*1</sup> Institute of Aviation Engineering, Civil Aviation University of China, Tianjin 300300, China

\* Corresponding author; E-mail: [mgong@cauc.edu.cn](mailto:mgong@cauc.edu.cn)

*Taken Xuanyun SW300PRO as the research plant, the influence of wake field on the safety of civil aviation aircraft during idling deicing is studied. A numerical model of idle wake flow is established, through which temperature and velocity distributions are analyzed, enabling demarcation of safe zones in the flow field. The Standard k-ε model is used to analyze the heat flow field of engine tail by comparing the numerical results of three typical turbulence models and the experimental data. Results indicate conical diffusion patterns of wake temperature and velocity radiating from the nozzle centerline, where flow divergence initiates at 0.6 m downstream. Thermal analysis reveals high-temperature zones ( $z < 0.9$  m,  $y < 0.5$  m) with 569-976 K, while low-temperature regions ( $z > 2.5$  m,  $y > 0.6$  m) maintain temperatures below 323 K. Hydrodynamic measurements show high-velocity cores ( $z < 0.2$  m,  $y < 0.2$  m) at 77-100 m/s, contrasting with low-speed areas ( $z > 0.9$  m,  $y > 0.2$  m) capped at <20 m/s. The human safety zone distance is:  $z > 2.5$  m,  $y > 0.5$  m. The research findings can provide valuable insights for accurately analyzing the thermal flow field of large civil aviation engine wake flows and for defining the safety zones for ground deicing operations during engine idle conditions.*

*Key words: Aero-engine; Idle deicing; Heat flow field; Wake flow*

## 1. Introduction

The high-temperature, high-speed flow field at the rear of aircraft engines is a direct factor affecting ground safety operations and is also a key element in enhancing aircraft deicing efficiency. In recent years, the Civil Aviation Administration has been actively promoting the idle deicing mode for aircraft. This mode involves performing deicing operations without shutting down the engine, imposing stricter requirements on the vehicle's operating distance, travel path, and designated area. Analyzing the thermal flow field characteristics at the rear of the engine under slow-roll conditions is crucial for accurately defining deicing safety zones, reducing the spray distance of deicing fluid, and ensuring the

effectiveness of the deicing process. This research is of great significance for improving deicing safety, increasing operational efficiency, and reducing deicing fluid consumption.

Some influence of environmental factors on wake gas behavior, and the distribution of wake flow fields under different flight parameters using discrete phase models [1-5]. Research focusing on three-dimensional wake flow models includes topics such as: the location and extent of infrared damage after engine exhaust, the characteristics of nozzle wake flows with different shapes, the effect of nozzles on the mixing and turbulence characteristics of free double jets, the impact of aircraft propulsion systems and engine wake structure on performance parameter variations, the effects of converging and conical nozzles on the flow field as described by parabolic equations, and the optimization of RANS models for jet aircraft flows [6-14].

In the field of computational fluid dynamics for wake flow studies, Fivel et al. [15] employed the Euler equations to estimate the three-dimensional invisible surface streamlines in conjunction with boundary layer solutions, using axisymmetric simulation techniques to predict heating rates. Bulat et al. [16] applied a turbulent model for separated flows to investigate and predict the effects of subsonic and transonic fluids on engine wake flows, with their turbulence model being applicable to turbulent flow problems in physical engineering. Teixeira et al. [17] used a dual-temperature solver and a vibrational nonequilibrium model to reduce discrepancies between numerical and experimental results, addressing hypersonic gas dynamics in spatial propulsion geometries. Reddy et al. [18] solved the Laplace equation describing potential flow using the GALERKIN method and a velocity-potential function. Wang et al. [19] utilized ANSYS Fluent to solve for symmetric flow fields, employing a second-order upwind scheme to discretize the fluxes of convective equations. Furthermore, Qi et al. [20] combined a mixed rupture model with turbulence inside the nozzle, illustrating the impact of internal nozzle flow on the wake flow composition.

In addition, some research methods in the thermal-fluid coupling study similar to the aircraft wake problem are also noteworthy, such as Xiong et al. [21] used Matlab to solve the partial differential equations of fluid-solid coupling to obtain the temperature distribution on the inner surface of the narrow rectangular specimen and fitted the empirical equations. Li et al. [22] combined Fluent, VC++ and APDL to conduct the thermal-fluid-solid coupling analysis of friction vice of the mating disk of axial piston pump of the electrostatic actuator of an aircraft. A coupled thermal-fluid-solid analysis was carried out to obtain the effects of fluid pressure and temperature on the temperature distribution and thermal deformation in the solid.

There has been considerable research both domestically and internationally on the wake flow characteristics at high Mach numbers and at certain flight altitudes, but studies on the ground-level thermal flow field at the engine rear during idle conditions are relatively limited. Despite significant progress in the numerical modelling of aircraft engine wake flows, research on turbulence models is still ongoing. The turbulence models commonly employed in the above studies include: the Standard  $k-\varepsilon$  model, the Realizable  $k-\varepsilon$  model, and the Low Reynolds  $k-\varepsilon$  model. In the study of aircraft engine flow problems, there is no consensus on the most appropriate turbulence model, and the models required for different research

problems still need further investigation and validation. The present study focuses on fluid-solid coupled heat transfer, using the COMSOL non-isothermal flow coupling interface as the solver for numerical simulations. Due to the complex modelling and substantial computational demands of large engines, corresponding data is still being acquired, while simplified models may introduce significant errors. Numerical analysis based on a real small-scale engine model is helpful for improving the accuracy of future large engine modelling and analysis.

The focus of the research is the temperature and velocity characteristics of the wake flow from the SW300PRO engine under idle mode, as well as the safety range for ground operations. Due to limited empirical data on turbulence models suitable for engine wake flows in idle state, the measured wake temperature and velocity values are compared with simulation results from three different turbulence models to validate the feasibility of the numerical model and determine the most suitable turbulence model. This allows for a numerical analysis of the dynamic characteristics of the thermal flow field at the engine rear. The findings can provide valuable insights for the study of wake flows from large civil aviation aircraft engines. In the next phase, physical models of the wake thermal flow field under fluid and heat transfer coupling will be constructed based on engine parameters from mainstream aircraft models such as the Boeing 737 and Airbus A330. This will support further modelling and wake flow characteristic analysis of major civil aviation engines, with a focus on the dynamic distribution of the deicing safety zone in the wake flow field during idle deicing conditions for commercial aircraft.

## **2. Model feasibility verification**

To verify the applicability of the numerical model used in this study and determine the most suitable turbulence model for simulating the wake flow field under idle conditions, this section compares the thermal flow field parameters collected from 15 regions of the wake flow experiment with the numerical simulation results from three different turbulence models to assess the feasibility of the numerical model.

### **2.1. Numerical simulation method**

Three-dimensional numerical simulations of the engine nozzle model were performed using COMSOL, with the control equations being the steady, weakly compressible RANS equations. To identify the appropriate turbulence model for the engine wake flow at idle, three turbulence models were employed: the Standard  $k-\varepsilon$  model, the Realizable  $k-\varepsilon$  model, and the Low Reynolds  $k-\varepsilon$  model.

#### **2.1.1. Geometric model and computational domain**

The theoretical study was based on the data of the Xuanyun SW300PRO engine, and a three-dimensional geometric model of the nozzle was created, as shown in Fig. 1. The simplified model of the nozzle was imported into the COMSOL software, retaining the tail cone section, as depicted in Fig. 2. A three-dimensional computational model for both the internal and external flow fields was established. The external computational domain was a cylinder, with the cylinder height  $h$  along the  $z$ -axis being 35 times the nozzle length, and the

radius  $R$  along the  $y$ -axis and  $x$ -axis being 10 times the nozzle inlet radius, as shown in Fig. 2 (a). The computational domain's layout is illustrated in Figs. 2 (a), where region 1 represents the nozzle, and region 2 represents the fluid region to be solved. The inlet is denoted as a-b, the outlet as e-f, and the outer boundaries of the flow field are shown as c-e and d-f.

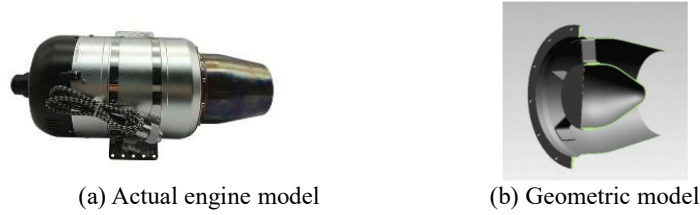


**Figure 1. Tail nozzle model.**

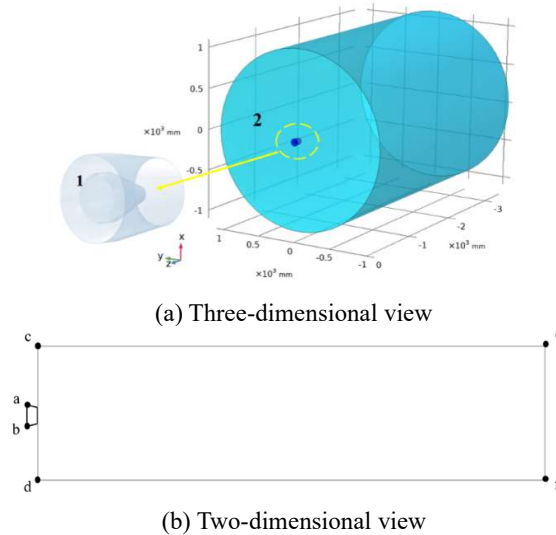


**Figure 2. Simplified structure of computation domain.**

### 2.1.2. Mesh generation and boundary conditions

The computational domain was meshed using tetrahedral elements, with mesh refinement applied in the vicinity of the nozzle exit region. Boundary layer meshes were also created around the tail cone and the domain boundaries. To validate mesh independence, grids with varying densities were compared, and the standard deviation was used to assess the mesh quality. The results showed that the average mesh quality for all three evaluated grids was above 0.8, which meets the requirements for fluid flow calculations [23], as shown in tab. 1. As an example, the simulation results using the Standard  $k-\epsilon$  model were taken to perform a mesh independence check, using the temperature values along the wake centerline. The results are shown in Fig. 3. Once the mesh density reached a certain level, the thermal flow field results became independent of the grid resolution, and the calculation results converged.

**Table 1. Meshing results of different models**

Model	Refined mesh		Finer mesh		Ultra-fine mesh	
	Mesh Elements	Element Quality	Mesh Elements	Element Quality	Mesh Elements	Element Quality
Standard $k-\epsilon$	13406	0.837	29135	0.840	62139	0.897
Realizable $k-\epsilon$	7540	0.928	12165	0.935	46206	0.959

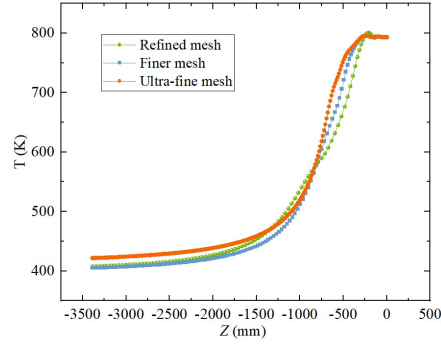


**Figure 3. Comparison of temperature results of three different mesh sizes.**

Based on the engine design, the SW300PRO engine operates at an idle speed of 33,000 RPM and a thrust of 30 kg under ambient conditions (288 K). The inlet temperature and velocity at the nozzle are specified, with the flow direction aligned with the nozzle axis.

The boundary conditions of the numerical model are as follows: The pressure at the computational domain outlet is set to standard atmospheric pressure, and the nozzle wall is assumed to be adiabatic with no-slip conditions. The inlet of the nozzle is treated as weakly compressible turbulent flow [24-25]. c-e and d-f are the boundaries of the air domain, set to open boundaries that allow the free exchange of heat and momentum.

The composition of the engine wake flow is complex, involving a mixture of jet and free stream flows. Since the experimental engine is positioned 1.2 m above the ground, the impact of the ground and flow field is simplified in this study [26]:

- 1). The engine exhaust gases are assumed to behave as an ideal gas, with complete combustion during the power cycle and no change in the chemical properties or specific heat ratio of the components.
- 2). The internal gas flow within the nozzle is treated as pure gas-phase flow, undergoing isentropic expansion.
- 3). Heat transfer through the nozzle wall and the effects of gravity on the air are neglected, as well as the infrared radiation effects of the exhaust gases.

### 2.1.3. Computational governing equation

In non-isothermal flow, pressure variations and viscous heating terms should be considered. The heat transfer equation for the fluid is as follows:

$$\rho C_p \mathbf{u} \cdot \nabla T = -(\nabla \cdot \mathbf{q}) + \boldsymbol{\tau} : \mathbf{S} - \frac{T}{\rho} \frac{\partial \rho}{\partial T} \mathbf{u} \cdot \nabla p + Q \quad (1)$$

$C_p$  is the specific heat capacity of the fluid,  $T$  is the absolute temperature,  $\mathbf{q}$  is the conductive heat flux,  $\boldsymbol{\tau}$  is the viscous stress tensor,  $\mathbf{S}$  is the strain rate tensor, and  $Q$  represents heat sources excluding viscous heating.

$$\mathbf{S} = \frac{1}{2} (\nabla \mathbf{u} + (\nabla \mathbf{u})^T) \quad (2)$$

The heat transfer equation for solids is:

$$\rho C_p \mathbf{u} \cdot \nabla T + \nabla \cdot (-k \nabla T) = Q + Q_{rad} \quad (3)$$

Where:  $\rho$  is the fluid density,  $C_p$  is the specific heat capacity of the fluid,  $\mathbf{u}$  is the velocity vector,  $T$  is the thermodynamic temperature,  $k$  is the thermal conductivity, and  $Q_{ted}$  represents the thermoelastic damping heat source.

For solving turbulence problems, the Reynolds-Averaged Navier-Stokes equations are employed. These equations neglect heat generation caused by viscous dissipation, while turbulent viscosity enhances the viscous transfer of momentum. This approach allows for the calculation of momentum transfer due to small-scale vortices that cannot be directly resolved, effectively addressing the high computational cost of standard equations within a reasonable computational budget [27].

In weakly compressible fluids,  $\partial\rho/\partial t = 0$ , the continuity equation and momentum equation are:

$$\nabla \cdot (\rho \mathbf{u}) = 0 \quad (5)$$

$$\rho(\mathbf{u} \cdot \nabla) \mathbf{u} = \nabla \cdot \left[ -p \mathbf{I} + \mu (\nabla \mathbf{u} + (\nabla \mathbf{u})^T) \right] + \mathbf{F} \quad (6)$$

Where  $\rho$  is the density of the fluid,  $\mathbf{u}$  is the velocity vector,  $p$  is the pressure,  $\mu$  is the dynamic viscosity, and  $\mathbf{F}$  is the volume force.  $\mathbf{I}$  is the identity matrix.

The governing equations for three models that are more typical in turbulence solution problems will be described here, with emphasis on the strengths and focus of the different models in describing the turbulence model in this paper, weakening the detailed description of the equations themselves, as follows.

(1) The Standard  $k$ - $\varepsilon$  model restricts the accuracy of calculations at high Reynolds numbers and when the boundary layer is in equilibrium, and the computational space can be limited for flows with large pressure gradients. In most cases, the Standard  $k$ - $\varepsilon$  model is preferred over other complex turbulence models in order to save computational resources, provided that the accuracy is guaranteed [28-29]. where the turbulent viscosity ( $\mu_T$ ) is calculated as:

$$\mu_T = \rho C_\mu \frac{k^2}{\varepsilon} \quad (7)$$

The transport equation of turbulent kinetic energy  $k$  is as follows:

$$\rho(\mathbf{u} \cdot \nabla) k = \nabla \cdot \left[ \left( \mu + \frac{\mu_T}{\sigma_k} \right) \nabla k \right] + P_k - \rho \varepsilon \quad (8)$$

The transport equation of turbulent dissipation rate  $\varepsilon$  is:

$$\rho(\mathbf{u} \cdot \nabla) \varepsilon = \nabla \cdot \left[ \left( \mu + \frac{\mu_T}{\sigma_\varepsilon} \right) \nabla \varepsilon \right] + C_{\varepsilon 1} \frac{\varepsilon}{k} P_k - C_{\varepsilon 2} \frac{\varepsilon^2}{k}, \varepsilon = \varepsilon_p \quad (9)$$

$$P_k = \mu_T \left[ \nabla \mathbf{u} : (\nabla \mathbf{u} + (\nabla \mathbf{u})^T) - \frac{2}{3} (\nabla \cdot \mathbf{u})^2 \right] - \frac{2}{3} \rho k \nabla \cdot \mathbf{u} \quad (10)$$

Where:  $C_\mu=0.09$ ,  $P_k$  is the generating phase,  $C_{\varepsilon 1}=1.44$ ,  $C_{\varepsilon 2}=1.92$ ,  $\sigma_\varepsilon=1.3$ ,  $\sigma_k=1$ .

(2) The Realizable  $k$ - $\varepsilon$  model is more accurate than the Standard  $k$ - $\varepsilon$  model for the description of some cylindrical flow conditions, but the wall functions are treated in the same way. The governing equation of the turbulent kinetic energy  $k$  is the same as that of the Standard  $k$ - $\varepsilon$  model, while the governing equation of the turbulent dissipation rate  $\varepsilon$  is different, as shown in equation (11):

$$\rho(\mathbf{u} \cdot \nabla) \varepsilon = \nabla \cdot \left[ \left( \mu + \frac{\mu_T}{\sigma_\varepsilon} \right) \nabla \varepsilon \right] + C_1 \rho S \varepsilon - C_2 \frac{\rho \varepsilon^2}{k + \sqrt{V \varepsilon}}, \varepsilon = \varepsilon_p \quad (11)$$

In equation (11),

$$C_1 = \max \left\{ 0.43, \frac{\eta}{5 + \eta} \right\}, \eta = \frac{Sk}{\varepsilon}, S = \sqrt{2S_{ij}S_{ij}}, S_{ij} = \frac{1}{2} \left( \frac{\partial \bar{u}_i}{\partial x_j} + \frac{\partial \bar{u}_j}{\partial x_i} \right)$$

Where:  $S_{ij}$  is the average strain tensor,  $\Omega_{ij}$  is the average rotation rate tensor,  $C_{\varepsilon 2}=1.9$ ,  $A_0=4$ ,  $\sigma_k=1$ ,  $\sigma_\varepsilon=1.2$ .

(3). In the Low Reynolds  $k-\varepsilon$  model, when the precision provided by wall functions is insufficient, the region near the wall is primarily governed by viscous effects. The governing equation for turbulent kinetic energy  $k$  remains identical to that in the standard  $k-\varepsilon$  model. However, the governing equation for the turbulent dissipation rate  $\varepsilon$  incorporates damping functions and is expressed as follows:

$$\rho(\mathbf{u} \cdot \nabla)\varepsilon = \nabla \cdot \left[ \left( \mu + \frac{\mu_T}{\sigma_\varepsilon} \right) \nabla \varepsilon \right] + C_{\varepsilon 1} \frac{\varepsilon}{k} P_k - f_\varepsilon C_{\varepsilon 2} \rho \frac{\varepsilon^2}{k} \quad (12)$$

The governing equation for turbulent viscosity is given by:

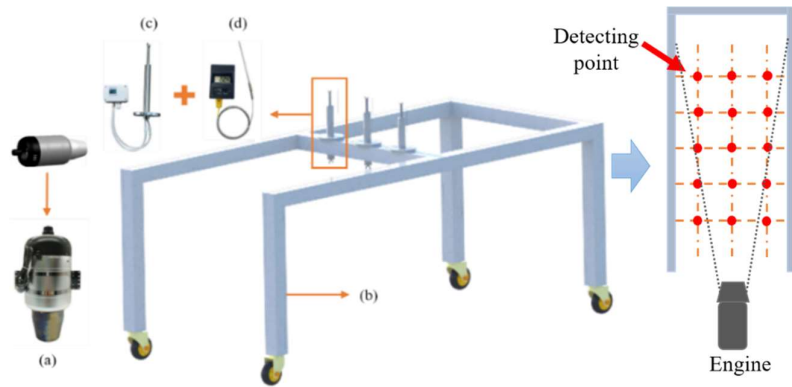
$$\mu_T = \rho f_\mu C_\mu \frac{k^2}{\varepsilon} \quad (13)$$

Here,  $P_k$  and other terms are consistent with those in Equation (10), while the governing equations for  $f_\mu$  and  $f_\varepsilon$  are as described in reference [30].

## 2.2. Experimental detection of wake thermal flow field

### 2.2.1. Experimental equipment and scheme

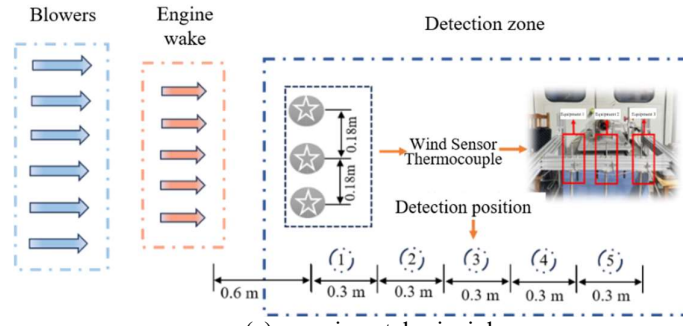
The experiment was conducted in an enclosed environment. The indoor equipment included a uniform wind supply machine and a Xuanyun SW300PRO turbofan engine operating at an idle speed of 33,000 RPM, as shown in Fig. 4. The detection instruments comprised an aluminium alloy test bench made of 6060 aluminium alloy (Euro standard) with dimensions of  $1.8 \times 0.75 \times 1.1$  m (length  $\times$  width  $\times$  height), a high-precision high-temperature wind speed transmitter (H8200B) with a measurement range of 0-110 m/s, and a K-type high-precision thermocouple WRNK-191 probe temperature sensor with a measurement range of 0-800 °C.



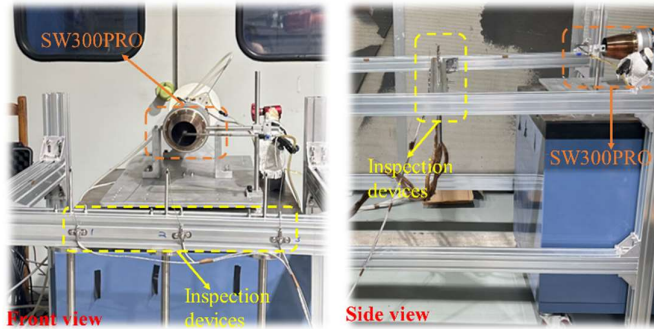
**Figure 4. Experimental equipment**

Figure 5 illustrates the experimental detection system. During the experiment, three thermocouples and a wind speed measuring device were arranged side by side, perpendicular to the wake flow direction, to perform measurements. Observations were conducted at five positions along the flow direction at distances of 0.6 m, 0.9 m, 1.2 m, 1.5 m, and 1.8 m from

the nozzle, recording data during stable idle operation for 10 seconds. The specific locations of the 15 detection points are marked with bold red dots in Figure 4. The test bench was positioned such that the central detection equipment was aligned horizontally with the nozzle centerline. The devices on either side were spaced 0.18 m apart, with a total detection length of 0.36 m. The detection setup is illustrated in Fig. 2. Due to the engine's rated exhaust temperature of 1033 K, which is considerably high, only the temperatures near the nozzle were measured.



(a) experimental principle



(b) Experimental detection diagram

**Figure 5. Experimental detection principle system**

### 2.2.2. Experimental Uncertainty

(1) Experimental environment. The uniform airflow generator in the laboratory, positioned above the engine, maintained an airflow velocity of 3 m/s, which introduced some influence on the wake flow temperature and velocity.

(2) Instrumentation. The K-type thermocouple had a reading uncertainty of  $\pm 0.5$  K, while the H8200B wind speed transmitter exhibited a measurement uncertainty of  $\pm 3\%$ .

(3) Experimental procedure. During the detection process, the laboratory environment had to cool down before adjusting the measurement positions. Multiple engine restarts led to variations in the indoor temperature, affecting data acquisition accuracy.

(4) Data processing. For experimental data, the average value over 10 seconds was taken as the measurement for each point. For simulation data, the average value within a circular area with a radius of 0.01 m around the measurement point was used as the corresponding value.

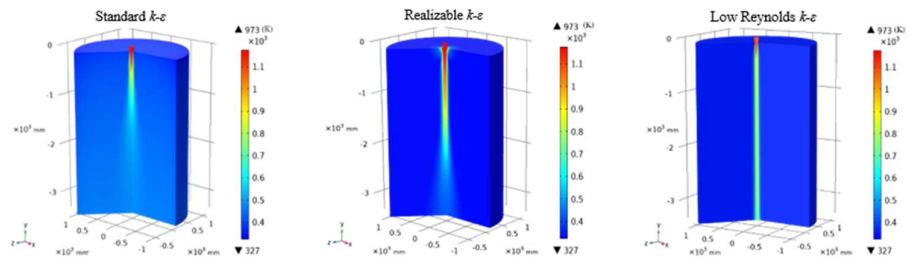
### 2.2.3. Model Validation Results

The temperature and axial velocity of the SW300PRO engine's wake flow were measured using the wake flow detection experiment to validate and compare the numerical

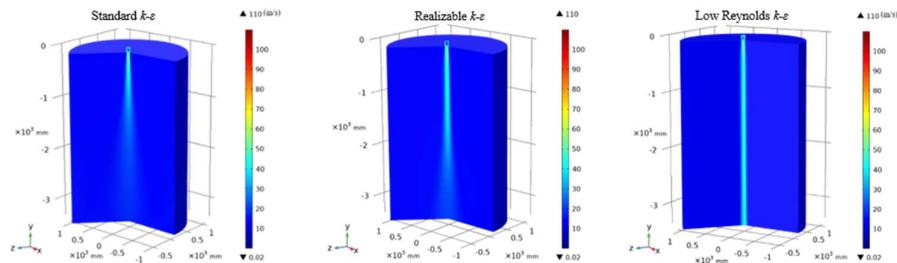
simulation capabilities of three turbulence models. As shown in Fig. 6 and Fig. 7, both the Realizable  $k-\varepsilon$  model and the Standard  $k-\varepsilon$  model closely match the experimental data, but in terms of temperature variation trends, the Standard  $k-\varepsilon$  model aligns more closely. In Fig. 7(b), all three models exhibit trends consistent with the experimental data, though the Standard  $k-\varepsilon$  model demonstrates better agreement.

To further validate the accuracy of the Standard  $k-\varepsilon$  model, a comparison was made between the temperature and velocity along the axis and at positions offset from the axis. Two parallel lines, each 0.18 m from the centerline on either side, were selected. A total of 15 points were compared at distances of 0.6 m, 0.9 m, 1.2 m, 1.5 m, and 1.8 m from the nozzle, as shown in Fig. 8. In Fig. 8(a), the temperature variation at the same detection points follows a consistent trend, with the difference most evident at the central axis. The simulation data at all three detection points are slightly higher than the experimental data, likely due to the increased convective heat transfer caused by the fan used in the experiment. In Fig. 8(b), the experimental and simulation results show consistent trends at the same detection points, with the closest agreement at detection point 2.

The governing equations of turbulence indicate that compared to the standard  $k-\varepsilon$  model, the calculation of turbulent dissipation rate in the Realizable  $k-\varepsilon$  model involves greater complexity and necessitates additional computations for turbulent viscosity coefficient. In the Low Reynolds  $k-\varepsilon$  model, the determination of both turbulent dissipation rate and turbulent viscosity coefficient requires further consideration of damping function effects. Considering computational accuracy and resource requirements, the Standard  $k-\varepsilon$  model demonstrates superior suitability for simulating engine idle conditions. Therefore, the Standard  $k-\varepsilon$  turbulence model was adopted in subsequent numerical investigations.



(a) Temperature distribution simulated by different models



(b) Velocity distribution simulated by different models

**Figure 6. The cloud image of temperature velocity distribution results simulated by three models**

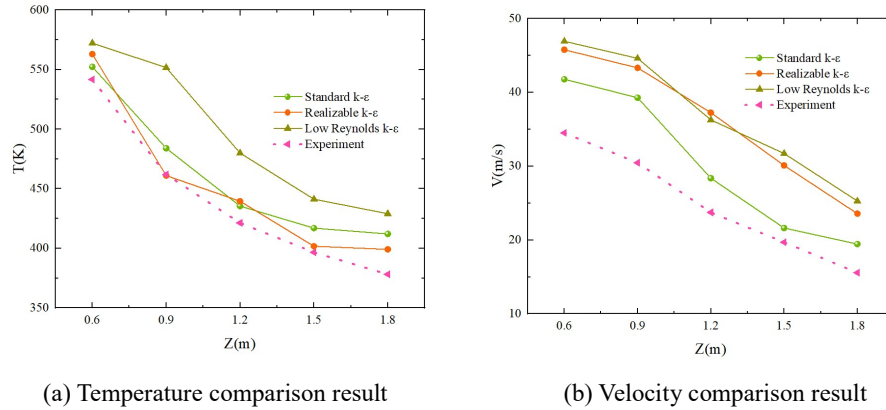


**Figure 7. Comparison between numerical simulation and experimental data of three turbulence models**

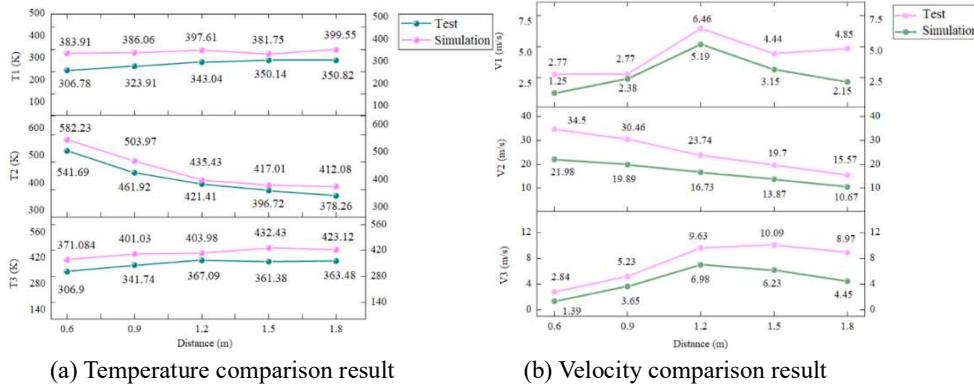


**Figure 8. Comparison between numerical simulation of Standard  $k-\epsilon$  model and experimental data**

### 3. Results and analysis

Based on the experimental analysis results, the optimized Standard  $k-\epsilon$  model was employed for wake flow field calculations, with wall treatment utilizing the standard wall function method. Open boundary conditions (zero normal stress) and pressure point constraints (standard atmospheric pressure) were added to the original model boundaries c-d, c-e, and e-f [31-32]. By analyzing the characteristics and distribution of the temperature and velocity fields in the wake flow under engine idle conditions, the safe operating area for the wake flow field was determined.

#### 3.1. Analysis of wake temperature field results

As shown in Fig. 9(a), the temperature field exhibits a steady-state distribution with uneven axial expansion. After exiting the nozzle, the airflow initially exhibits axial rotational symmetry over a certain distance, with the highest temperature observed at the center. As the axial distance increases, the temperature gradually decreases, with the region experiencing significant temperature variation concentrated within a range of 315.4-976.0 K. The maximum temperature near the nozzle reaches 976.0 K, and the core high-temperature range of the wake is 569.1-976.0 K. During numerical simulation, a simplified turbulence model

was employed, and the influence of ambient gravity was neglected. Additionally, turbulence in high-speed flows generates vortices in various directions, causing the wake centerline orientation to shift. The center temperature of each cross-section gradually moves towards the negative  $y$ -axis and positive  $z$ -axis directions. The engine wake constitutes an unstable synthetic jet, which has a certain impact on the heat transfer coefficient [33].

In Fig. 9(b), the degree and specific variations of temperature diffusion across each section are not particularly distinct. To analyze the wake temperature field characteristics more clearly, the temperature distribution of each section is presented in the form of three-dimensional mappings, as shown in Fig. 10. From this figure, it is evident that the wake distribution conforms to a Gaussian profile, with the highest temperature at the center, gradually diffusing outward. The temperature gradient exhibits significant changes within  $z < 0.5\text{m}$ , declining rapidly. In the region where  $z > 2.5\text{m}$ , the temperature changes slowly, forming a low-temperature zone with a minimum temperature of 325.0 K. The temperature diffusion along the  $y$ -axis and  $x$ -axis directions is relatively limited, with high-temperature regions concentrated within  $\pm 0.2\text{ m}$  of both axes. Figure 11 shows that the temperature distribution at various distances from the nozzle, specifically at cross-sections located 0.3 m, 0.9 m, 1.5 m, and 2.1 m along the  $z$ -axis. From the figure, it can be observed that at  $z = 0.3\text{ m}$ , the high-temperature danger zone forms a core-centered distribution. Closer to the nozzle, the cloud diagram exhibits more pronounced peaks, with rapid and uniform temperature changes spreading outward, confined to a smaller area. In contrast, for  $z > 0.9\text{m}$ , the temperature gradient diminishes as the distance from the nozzle increases, with the affected area expanding and the central temperature gradually diffusing unevenly towards the surroundings.

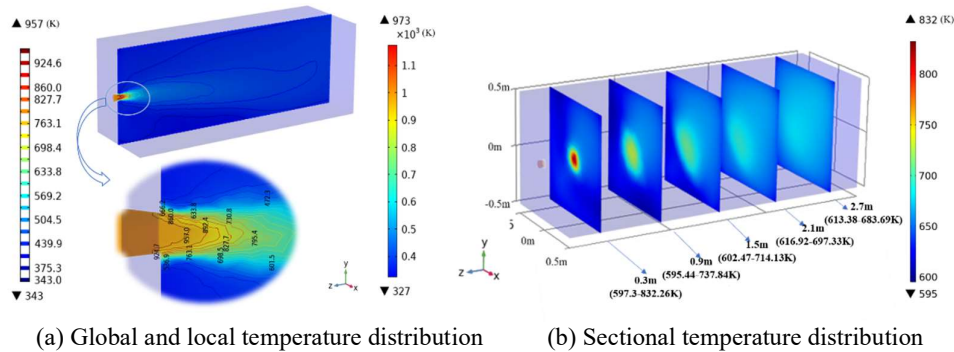


**Figure 9. Engine wake temperature distribution**

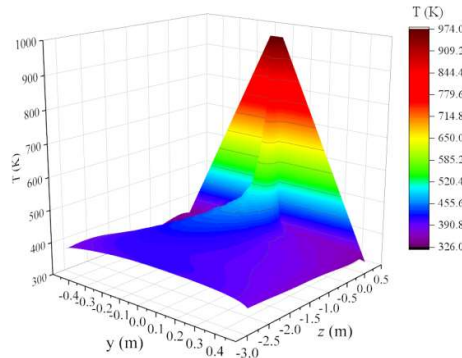


**Figure 10. Temperature distribution of engine wake  $y$ - $z$  section**

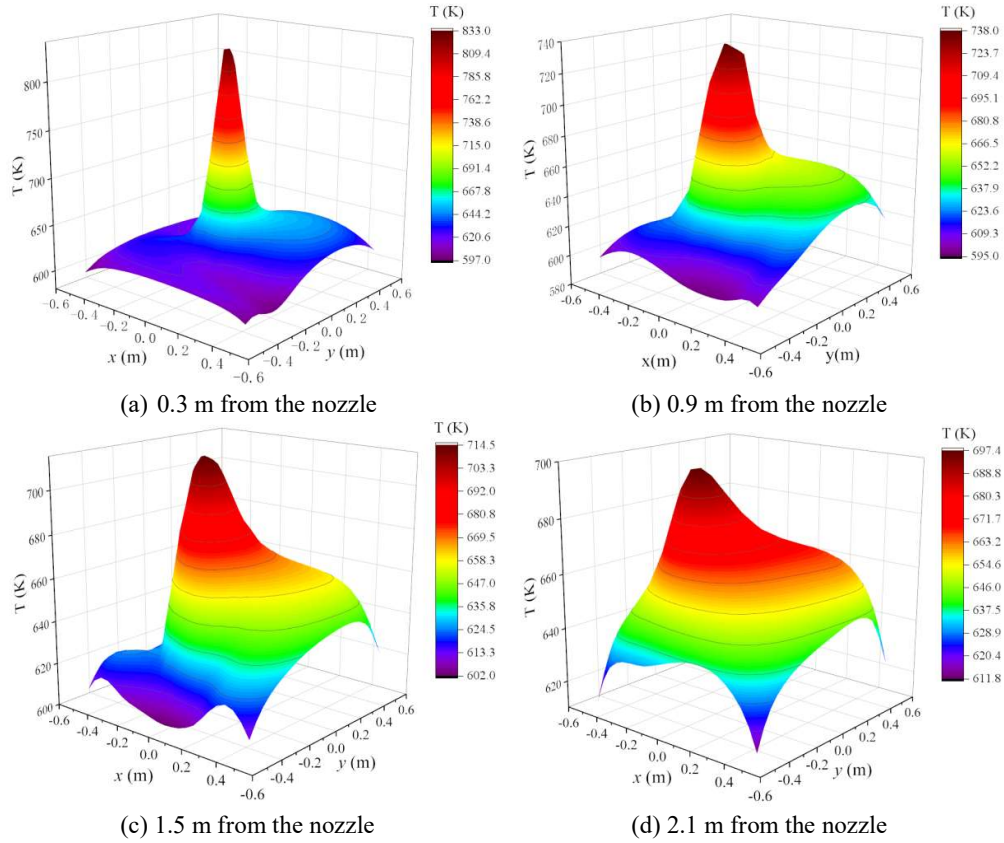


**Figure 11. Temperature distribution of  $x$ - $y$  section from different positions of nozzle**

### 3.2. Analysis of wake velocity field results

As shown in Fig. 12, the isothermal lines in the flow field are densely distributed at the nozzle, with concentrated regions of velocity change, consistent with the flow characteristics of free turbulent jets in low Reynolds number mixed flows [34-35]. Additionally, Weiss et al. [36] demonstrated that numerical simulations of mixed flows better align with real-world conditions. The velocity impact range along the  $y$ -axis and  $x$ -axis is relatively small and similar, while the range along the  $z$ -axis is significantly larger. The velocity gradually decreases along the nozzle axis, with the high-speed region confined within  $z < 0.2$  m,  $y < 0.1$  m,  $x < 0.1$  m, where the velocity ranges from 77 to 110 m/s. From the zoomed-in section, it is evident that the velocity within the nozzle increases progressively. The convergent nozzle design reduces the outlet cross-sectional area under constant flow, thereby increasing velocity. In the low-speed region ( $0.5$  m  $< z < 2.1$  m), the maximum velocity does not exceed 20 m/s.

In Fig. 12(b), the velocity distribution of the wake exhibits an uneven normal distribution, with substantial variation in the shape of the velocity contours across different sections. The jet's trajectory deflects toward the fourth quadrant of the  $x$ - $y$  plane. Beyond  $z > 0.9$  m, the wake is mostly mixed with the surrounding environment, showing no significant velocity changes. Sharma et al. [37] found that synthetic jets exhibit some discrepancies compared to steady jets in terms of the centerline velocity decay rate, with jet diffusion

following a nonlinear growth pattern. This suggests that after exposure to high-temperature and high-speed conditions, the internal structure of the fluid undergoes changes, leading to centerline deflection. These findings align with the numerical simulation results of this study. Some researchers have numerically simulated the characteristics of wakes and concluded that interactions within the internal fluid structure cause vortex displacement, transforming the axial velocity of vortices into jet flow and increasing the backward diffusion of vortices [34]. However, the actual flow rate field jet is still dynamic and complex, and the numerical model needs to be constantly revised and optimized, and there is a big difference between the research results and the two-dimensional model, and the three-dimensional simulation is more consistent with the actual situation.

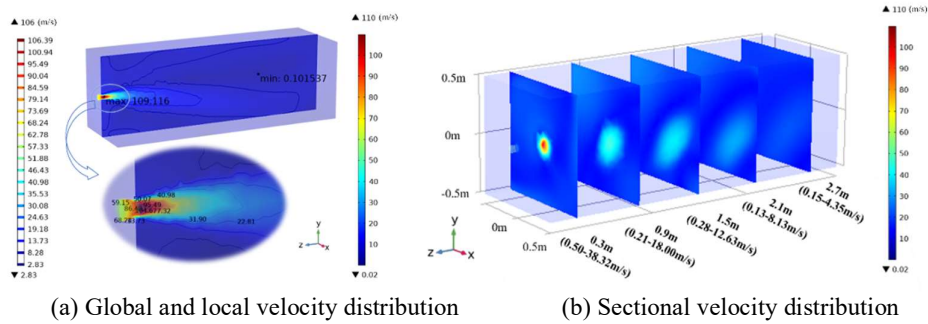


**Figure 12. Engine wake velocity distribution**

In Fig. 13, the airflow velocity experiences a rapid drop over a short distance, decreasing from 110 m/s to 32 m/s. Beyond this point, the temperature gradient changes more gradually, remaining nearly uniform. The radial range of high-speed airflow along the axial direction is confined to 0.1 m, with the overall influence of gas velocity being relatively limited. To provide a clearer explanation and analysis of velocity characteristics, two  $y$ - $x$  cross-sections near and far from the nozzle were examined, as shown in Fig. 14. From Fig. 14, it can be observed that the radial influence of wake velocity near the nozzle is relatively small, characterized by a narrow high-speed jet. Velocity decreases rapidly outward from the high-speed core. In contrast, the velocity distribution in the distant wake appears more uniform, with velocity spreading evenly in all directions and showing no significant differences in magnitude.

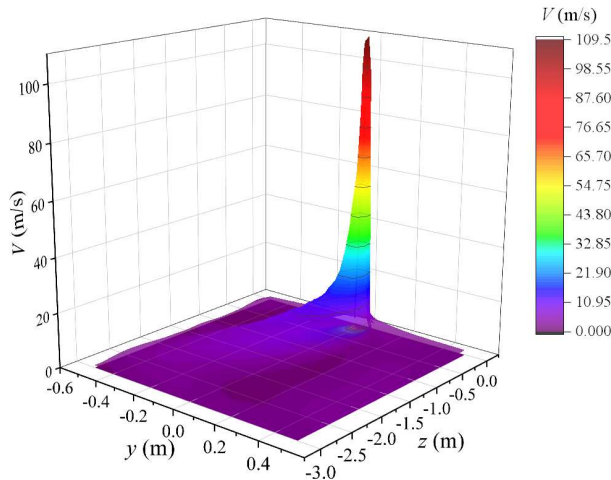
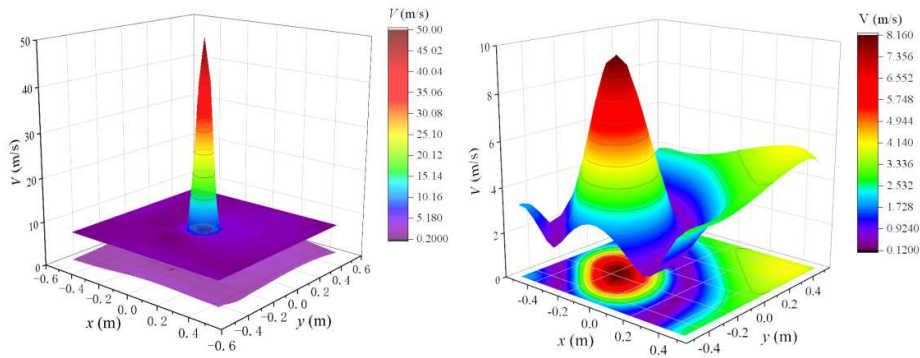


**Figure 13. Velocity distribution of y-z section of engine wake**



(a) 0.2 m from the nozzle

(b) 2.1 m from the nozzle

**Figure 14. Velocity distribution of x-y section of engine wake from different positions of nozzle**

Based on the analysis of the wake temperature and velocity fields, cross-sectional views from different directions and perspectives were used to evaluate the results in reference to the MH5001-2013 Civil Airport Technical Standards for deicing safety zone planning and relevant U.S. wake separation standards. According to these standards, the human heat tolerance temperature is below 323 K, the safe operating environment temperature for specialized equipment should not exceed 313 K, and the maximum tolerable wind speed should not exceed 29 m/s. [38]

From this analysis, the thermal flow field distribution of small engines and the safe operational zones for personnel can be illustrated, as shown in Fig. 15. The above analysis indicates that the temperature and velocity effects of the wake are similar in the y and x directions, with the y-direction influence range being slightly larger than that in the x direction. Thus, the y-direction results are used to represent the x-direction results. Fig. 14 illustrates the wake thermal flow field distribution in the y-z plane. Since the range of wake influence along the y-axis is relatively small, a fan-shaped division with a 30° angle to the z-axis is applied for the analysis.

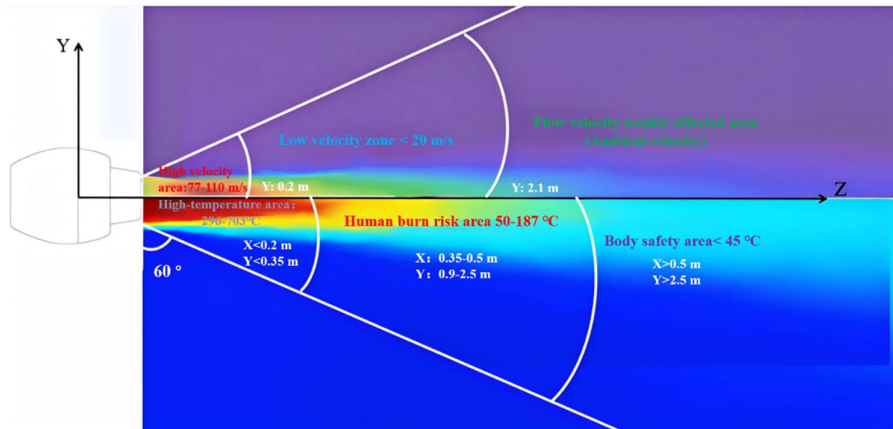


**Figure 15. Schematic diagram of engine wake heat flow field**

As shown in Fig. 15, the temperature zones are categorized as follows:

- (1) High-temperature region:  $z < 0.7$  m,  $y < 0.35$  m, with a temperature range of 569-976

K.

(2) Moderately high-temperature region (risk of human burns):  $0.9 \text{ m} < z < 2.5 \text{ m}$ ,  $y < 0.5 \text{ m}$ , with a temperature range of 323-569 K.

(3) Low-temperature region (safe operational zone for humans):  $z < 2.5 \text{ m}$ ,  $y < 0.7 \text{ m}$ , with temperatures below 313 K.

The velocity zones are defined as:

(1) High-velocity region:  $z < 0.2 \text{ m}$ , with a velocity range of 77-110 m/s.

(2) Low-velocity region:  $0.2 < z < 2.1 \text{ m}$ ,  $y < 0.3 \text{ m}$ , with velocities below 20 m/s.

(3) Ambient velocity region:  $z > 2.1 \text{ m}$ , with negligible flow velocity influence.

Safe operational zone for humans:  $z > 2.1 \text{ m}$ ,  $y > 0.5 \text{ m}$ . High-temperature and high-velocity hazardous zone:  $y < 0.2 \text{ m}$ ,  $z < 0.2 \text{ m}$ .

#### 4. Conclusions

To investigate the impact of idle deicing jet wake fields on operational safety for civil aviation aircraft, the study takes the Xuanyun SW300PRO turbofan engine as the research subject. A numerical model of the pure gas-phase flow under idle conditions was established to analyze the distribution and variation of wake temperature and velocity fields, as well as to delineate the thermal flow field's safety zones. By comparing the numerical results of three typical turbulence models with experimental data, the Standard  $k-\varepsilon$  turbulence model was selected for further analysis of the engine's thermal wake field. Based on this, the numerical model of the wake flow field was refined, enabling the study of temperature and velocity characteristics of the wake and the definition of appropriate safety zones for idle deicing operations on the ground. The following conclusions were drawn:

(1) Validation results indicate that among the three turbulence models evaluated, the Standard  $k-\varepsilon$  model is the most suitable for analyzing the flow field under idle conditions of the engine. This model effectively resolves the temperature and velocity distributions in the wake flow field with reasonable accuracy while conserving computational resources.

(2) The wake thermal flow field exhibits a conical diffusion pattern, expanding outward from the nozzle. The distribution on the  $x$ - $y$  cross-section aligns with a Gaussian distribution, with the highest value at the center, gradually decreasing toward the edges. Compared to the velocity field, the thermal field demonstrates a more extensive range of influence. The jet velocity dominates near the nozzle, with a steep decline in gradient further downstream.

(3) The high-temperature core region of the wake is defined as:  $z < 0.7 \text{ m}$ ,  $y < 0.35 \text{ m}$ ,  $x < 0.2 \text{ m}$ , with core temperatures ranging from 569.1 K to 976.0 K. The safe operational area for personnel is defined as:  $z > 2.5 \text{ m}$ ,  $y > 0.5 \text{ m}$ ,  $x > 0.5 \text{ m}$ , where the temperature does not exceed 323 K.

(4) The high-velocity core region is defined as:  $z < 0.2 \text{ m}$ ,  $y < 0.3 \text{ m}$ ,  $x < 0.2 \text{ m}$ , with velocity ranging from 77 m/s to 100 m/s. The safe operational area for personnel is defined as:  $0.5 < z < 2.1 \text{ m}$ ,  $y > 0.3 \text{ m}$ , where the velocity does not exceed 20 m/s. Beyond  $z > 2.1 \text{ m}$ , the fluid mixes with the surrounding environment, causing no significant impact.

The research methodology presented in this study provides a valuable reference for investigating the wake flow fields of civil aviation engines. Future work will focus on

modeling and analyzing the wake characteristics of mainstream civil aviation engines, such as those used in Boeing 737-800 and Airbus A320, based on their engine parameters. This ongoing research aims to deepen the understanding of the dynamic distribution of safe operational zones in the wake flow field during idle engine deicing operations for civil aircraft.

## Acknowledgment

The authors are grateful for financial support from the Fundamental Research Funds for the Central Universities, China (No. 3122023043).

## Nomenclature

<p><b>Symbols</b></p> <p><math>x</math> Length in the <math>x</math>-direction, [m]  <math>y</math> Length in the <math>y</math>-direction, [m]  <math>z</math> Length in the <math>z</math>-direction, [m]  <b>F</b> body force, [N]  <math>p</math> pressure, [Pa]  <math>S</math> strain rate tensor, [1/s]</p>	<p><math>T</math> temperature, [K]  <b>u</b> velocity vector, [m/s]  <math>V</math> velocity, [m/s]  <b>Greek symbols</b>  <math>\rho</math> density, [kg/m<sup>3</sup>]  <math>\mu</math> dynamic viscosity, [kg m<sup>-1</sup>s<sup>-1</sup>]</p>
--	---

## References

- [1] Hofacker, W., Huchler, M., Analysis of the Flow Field in the HERMES Cabin, *International Conference on Environmental Systems*, USA, 1990.
- [2] Mzad, H., Elguerra, M., Theoretical and Experimental Investigation of Compressible Flow through Convergent-Divergent Nozzles, *Advanced Materials Research*, 452(2012), pp. 1277-1285.
- [3] Lin, P., et al., Numerical Simulation of In-Nozzle Flow Characteristics under Flash Boiling Conditions, *International Journal of Multiphase Flow*, 127(2020), 103275.
- [4] Daniels, T., et al., Simulation of Airborne Radiometric Detection of Wake Vortices, *IEEE Transactions on Geoscience and Remote Sensing*, 53(2015), 12, pp. 6336-6343.
- [5] Yuan, Y., et al., Numerical Study on Infrared Radiation Characteristics of Stealth Coating for Turbofan Engine Tail Nozzle, *Energies*, 15(2022), 20, 7486.
- [6] Feng, Y. S., Infrared Characteristics and Flow Field of the Exhaust Plume outside Twin Engine Nozzle, *International Conference on Optoelectronics and Microelectronics Technology and Application*, 10244(2017), 133586625.
- [7] Jassim, E. I., CFD Study on Particle Separate on Performance by Shock Inception During Natural Gas Flow in Supersonic Nozzle, *Progress in Computational Fluid Dynamics, International Journal*, 16(2016), 5, pp. 300-312.
- [8] Morris, E. M., et al., Particle Image Velocimetry Measurements of Turbulent Jets Issuing from Twin Elliptic Nozzles with Various Orientations, *Journal of Fluids Engineering*, 143(2021), 2, 021501.
- [9] Arif, I., et al., Computational Analysis of Integrated Engine Exhaust Nozzle on a Supersonic Fighter Aircraft, *Journal of Applied Fluid Mechanics*, 11(2018), 6, pp. 1511-1520.
- [10] Arif, I., et al., Analytical Modelling and Validation of a Turbofan Engine at Design Conditions, *AIAA Scitech*

- 2019 Forum, AIAA, San Diego California, 2019.
- [11] Walimbe, P., et al., Flow Characteristics and Novel Applications of Synthetic Jets-A Review, *Journal of Heat Transfer*, 143(2021), 11, 112301.
  - [12] Kang, G. Q., Wang, Q., Numerical Simulation of Jet Flow Field of a V-Shaped Trailing Edge Split Exhaust Nozzle, *Journal of Aerospace Power*, 26(2011), 1, pp. 154-160.
  - [13] Eri, Q., et al., Numerical Investigation of Jet Control Using Two Pulsed Jets under Different Amplitudes, *Energies*, 15(2022), 2, 640.
  - [14] Hu, J., et al., Numerical Simulation and Experiment on Assemble Nozzles' Flow Field in Laser Cutting, *Materials Science Forum*, 663(2011), pp. 1302-1305.
  - [15] Fivel, H., An Approximate Method for the Calculation of Flow Field Profiles, *SAE Technical*, 7(1987), 110090535.
  - [16] Bulat, M. P., Bulat, P. V., Comparison of Turbulence Models in the Calculation of Supersonic Separated Flows, *World Applied Sciences Journal*, 27(2013), 10, pp. 1263-1266.
  - [17] Teixeira, O., Pascoa, J., Hypersonic Flow Simulation towards Space Propulsion Geometries, *SAE Aero-Tech Europe*, 2(2020), 2, pp. 803-810.
  - [18] Reddy, S., Deb, A., An Improved Finite Element Formulation for Potential Flow Problems Using a Kutta Condition, *SAE International Journal of Aerospace*, 15(2022), 1, pp. 99-117.
  - [19] Wang, Y., et al., Flow and thrust characteristics of an expansion-deflection dual-bell nozzle, *Aerospace Science and Technology*, 123(2022), 107464.
  - [20] Qi, W. L., et al., Numerical Investigation of the Characteristics of Spray/Wall Interaction with Hybrid Breakup Model by Considering Nozzle Exit Turbulence, *SAE International Journal of Engines*, 12(2019), 1, pp. 31-44.
  - [21] Xiong, K., et al., Temperature Distribution of a Test Specimen with High-Speed Heat Airflow Passing through, *Thermal Science*, 22(2022), 2527.
  - [22] Li, Y. H., et al., Thermal-fluid-structure coupling analysis for valve plate friction pair of axial piston pump in electrohydrostatic actuator (EHA) of aircraft, *Applied Mathematical Modeling*, 47(2017), 839.
  - [23] Tyliczszak, A., et al., Numerical Analysis of Non-Excited and Excited Jets Issuing from Non-Circular Nozzles, *International Journal of Heat and Fluid Flow*, 94(2022), 108944.
  - [24] Mzad, H., Elguerri, M., Theoretical and Experimental Investigation of Compressible Flow Through Convergent-Divergent Nozzles, *Advanced Materials Research*, 452(2012), pp. 1277-1285.
  - [25] Thermodynamics of Incompressible and Compressible Fluid Flow. SAE AIR 1168/1A-2019, 2019, 156.
  - [26] Liu, Y. W., et al., Numerical Simulation of Jet Interaction Flow Field with Different Flow Rates, *Journal of Physics: Conference Series*, 2364(2022), 1, 012065.
  - [27] Sun, X. L., et al., Flow Characteristics of Double Serpentine Convergent Nozzle with Different Inlet Configuration, *Journal of Engineering for Gas Turbines and Power*, 140(2018), 8, 082602.
  - [28] Krastev, V., et al., Some Developments in DES Modeling for Engine Flow Simulation, *SAE Technical*, 24(2015), 2414.
  - [29] Bharath, M., et al., Air Percolation Analysis for Multiphase Flow Using Volume of Fluid Approach, *SAE International Journal of Aerospace*, 14(2021), 1, pp. 95-113.
  - [30] Shih, T. H., et al., A New  $k-\varepsilon$  Eddy Viscosity Model for High Reynolds Number Turbulent Flow, *Computer and Fluid*, 24(1995), 3, pp. 227-238.
  - [31] Mu, G. Z., et al., An Analysis of Jet Noise Characteristics in the Compressible Turbulent Mixing Layer of a Standard Nozzle, *Machines*, 10(2022), 10, pp. 826.
  - [32] Eri, Q., et al., Numerical Investigation of Jet Control Using Two Pulsed Jets under Different Amplitudes,

*Energies*, 15(2022), 2, 640.

- [33] Masovic, D., et al., Directivity Measurements of Low Frequency Sound Field Radiated from an Open Cylindrical Pipe with a Hot Mean Flow, *SAE*, 1(2016), 1822.
- [34] Dghim, M., et al., Near Wake Development of a Wing Tip Vortex under the Effect of Synthetic Jet Actuation, *Aerospace Science and Technology*, 54(2016), pp. 88-107.
- [35] Guimarães, T., et al., Complex Flow Generation and Development in a Full-Scale Turbofan Inlet, *Journal of Engineering for Gas Turbines and Power*, 140(2018), 8, 082606.
- [36] Weiss, A. G., et al., Flow Regime and Reynolds Number Variation Effects on The Mixing Behavior of Parallel Flows, *Experimental Thermal and Fluid Science*, 134(2022), 110619.
- [37] Sharma, P., et al., A Critical Review on Flow and Heat Transfer Characteristics of Synthetic Jet, *Transactions of the Indian National Academy of Engineering*, 7(2022), 1, pp. 61-92.
- [38] Doll, U., et al., Non-Intrusive Flow Diagnostics for Unsteady Inlet Flow Distortion Measurements in Novel Aircraft Architectures, *Progress in Aerospace Sciences*, 130(2022), 100810.

Paper submitted: 28.12.2024

Paper revised: 01.03.2025

Paper accepted: 07.03.2025